PHYSICAL REVIEW C VOLUME 23, NUMBER 3 MARCH 1981

Time-dependent Hartree-Fock collisions of $^{16}O + ^{93}Nb$ at $E_{lab} = 204$ MeV

K. R. Sandhya Devi
W. K. Kellogg Radiation Laboratory, California Institute of Technology, Pasadena, California 91125

M. R. Strayer
Department of Physics and Wright Nuclear Structure Laboratory, Yale University, New Haven, Connecticut 06520

J. M. Irvine
Department of Theoretical Physics, University of Manchester, Manchester M13 9PL, United Kingdom and Daresbury Laboratory, Science Research Council Daresbury, Warrington WA4 4AD, United Kingdom

K. T. R. Davies
Physics Division, Oak Ridge National Laboratory, Oak Ridge, Tennessee 37830
(Received 26 August 1980)

Time-dependent Hartree-Fock computations are performed for the $^{16}O + ^{93}Nb$ system at a laboratory bombarding energy of 204 MeV. We employ an approximation in which the components of the wave functions perpendicular to the reaction plane are held constant in time. At this energy the total reaction cross section is comprised of approximately equal amounts of fusion and deep inelastic scattering. Fusion is found for those entrance channel angular momenta between $l = 31\hbar$ and $l = 75\hbar$; strongly damped inelastic scattering is found above and below this region. The angular momentum excited in the inelastic fragments is shown to have a different character in the different inelastic branches and this behavior could conceivably be used as a test to experimentally prove or disprove the existence of the fusion window.

[NUCLEAR REACTIONS $^{16}O(^{93}Nb,x)$ in time-dependent Hartree-Fock approximation. Fusion and deep-inelastic scattering.]

I. INTRODUCTION

The successful representation of heavy-ion collisions within the time-dependent Hartree-Fock (TDHF) theory[1] has stimulated a variety of investigations employing both two[2-5] dimensional (2D) and three[6,7] dimensional (3D) models. These studies have focused principally on fusion in lighter heavy-ion systems[7-11] and deeply inelastic scattering in very heavy systems[12-18] over a wide range of bombarding energies.

At energies of a few MeV per particle above the Coulomb barrier, TDHF calculations of lighter heavy-ion reactions exhibit highly inelastic scattering for large impact parameters less than grazing and for nearly head-on impact parameters. Fusion is usually observed for a range of impact parameters intermediate between these two regions. In these light systems, the magnitude and energy dependence of the theoretical fusion excitation functions are in general agreement with the experimental data.[7,9,11,16]

TDHF studies[12-18] have also been performed for several systems whose composite mass number is greater than 200. For these systems, and in particular for the Kr induced reactions,[12,15] the calculated outgoing fragment kinetic energies, scattering angles, and mean masses and charges are qualitatively in good agreement with experiment. However, mass and charge distribution widths are incorrectly given.[12,19] Fusion is also observed in these calculations[15,16] but there are discrepancies between the theoretical and experimental results. On the other hand, the experimental fusion cross section is less than 10% of the total reaction cross section.[20]

In the present study, we report TDHF calculations of the $^{16}O + ^{93}Nb$ collision at a laboratory bombarding energy of 204 MeV. Our calculations are performed using the approximation in which the components of the wave functions perpendicular to the reaction plane are held constant in time (frozen approximation), thereby reducing the 3D theory to a set of 2D equations.[4,5] This represents a region of mass which is intermediate between the heavy systems where deep inelastic processes dominate the reaction,[21] and the light systems where fusion is the major component of the reaction cross section.[22] Experimentally, at this energy, the $^{16}O + ^{93}Nb$ total reaction cross section is comprised of approximately equal parts of fusion and deeply inelastic scattering.[23] Thus the study of this system is expected to provide useful information on the interplay of fusion and other highly

inelastic processes within the TDHF theory. In Sec. II we briefly describe the model using the finite-range nonlocal Skryme II potential of Ref. 24. Details of this reduction will be given elsewhere.[25] In Sec. III we present the main results of our calculations, and in Sec. IV we discuss the principle limitations and conclusions of our study.

II. 2D TDHF EQUATIONS

In this section, we briefly describe the reduction of the 3D equations to 2D form using the frozen approximation.[4,5] For a detailed account of the application of TDHF theory to describe heavy ion reaction, we refer the reader to relevant literature.[1-3,6,7,10]

For collisions in which a reaction plane can be defined (e.g., collisions with two principal fragments), we make the approximation that wave functions $\Psi^q_\lambda(\vec{r},t)$ are given by

$$\Psi^q_\lambda(\vec{r},t)=\chi_\eta(\vec{r}_\perp)\phi^q_{\lambda\eta}(\vec{r}_\parallel,t), \tag{1}$$

where $\vec{r}_\parallel$ are the coordinates which lie in the reaction plane and $\vec{r}_\perp$ is the coordinate which is perpendicular to this plane. The index λ labels all of the quantum numbers needed in order to completely specify a single particle state of charge q. Equation (1) assumes an approximation in which the wave function is factorized into the product of a component which is perpendicular to the reaction plane and independent of time, and a component which is in the reaction plane and varies in time during the collision. In our present work, we have taken $\chi_\eta(\vec{r}_\perp)$ to be a harmonic oscillator function, where η denotes the principal quantum number. The TDHF equations follow in a straightforward way from the stationarity of the many-body action as discussed in previous work.[26] We employ the finite range, nonlocal Skyrme-II force which allows us to write the action in terms of the Hamiltonian density $H(\vec{r},t)$ as ($\hbar=1$)

$$\mathcal{S}=\int dt\int d\vec{r}_\parallel\Big[H(\vec{r}_\parallel,t)-i\sum_{\lambda q\eta}\phi^{q*}_{\lambda\eta}(\vec{r}_\parallel,t)\dot{\phi}^q_{\lambda\eta}(\vec{r}_\parallel,t)\Big],$$

$$H(\vec{r}_\parallel,t)=\int d\vec{r}_\perp H(\vec{r},t), \tag{2}$$

with the Hamiltonian density $H(\vec{r},t)$ specified in terms of the kinetic energy density τ, the two and three body zero-range potential energy density W, and the Coulomb and finite-range Yukawa nuclear potential energy densities as

$$H(\vec{r},t)=\frac{1}{2m}\tau(\vec{r},t)+W(\vec{r},t)+\frac{e^2}{2}\int d\vec{r}'\rho_p(\vec{r},t)\rho_p(\vec{r}',t)/(|\vec{r}-\vec{r}'|)$$
$$+\frac{a_0}{2}\int d\vec{r}'\frac{e^{-|r-r'|/a_0}}{|\vec{r}-\vec{r}'|}\{V_L[\rho_p(\vec{r},t)\rho_p(\vec{r}',t)+\rho_n(\vec{r},t)\rho_n(\vec{r}',t)]+V_u[\rho_n(\vec{r},t)\rho_p(\vec{r}',t)+\rho_p(\vec{r},t)\rho_n(\vec{r}',t)]\}. \tag{3}$$

(Note that the potential W also includes the velocity dependent Skyrme terms.) The potential energy density W, the definitions of ρ,τ, and $\vec{J}$, and the parameters of the modified Skyrme II force are explicitly given in Table I. The stationarity of the action with respect to variations in the single particle state $\phi^q_{\lambda\eta}(\vec{r}_\parallel,t)$ determine the TDHF single particle equations

$$\frac{\delta\mathcal{S}}{\delta\phi^{q*}_{\lambda\eta}(\vec{r}_\parallel,t)}=0,$$
$$\Big[h^q_\eta(\vec{r}_\parallel,t)-i\frac{d}{dt}\Big]\phi^q_{\lambda\eta}(\vec{r}_\parallel,t)=0, \tag{4}$$

where h^q_η is the TDHF single particle Hamiltonian. Instead of solving these equations directly we adopt the numerical procedure[2] of using a discrete representation of the action integral in (2) and require that this quantity be stationary with respect to variations of the wave function $\phi^q_{\lambda\eta}$ at specific mesh points, i.e., we discretize the action before taking variations. This procedure leads to a set of two-dimensional finite-difference TDHF equations

$$\sum_{\alpha',\beta'}h^q_\eta(\alpha,\beta,\alpha',\beta';t)\phi^q_{\lambda\eta}(\alpha',\beta';t)=i\dot{\phi}^q_{\lambda\eta}(\alpha,\beta;t), \tag{5}$$

where α,β are indices corresponding to the discrete representation of the Cartesian coordinates defining the reaction plane. Given that the solutions to Eq. (5), at some instant of time ($t=0$), are the static Hartree-Fock solutions $\xi^q_{\lambda\eta}(\vec{r}_\parallel)$ those at a later time are obtained by repeated application of an exponential time evolution operator.[7] Thus given the solution at a time t, the solution at a time $t+\Delta t$ is

$$\phi^q_{\lambda\eta}(t+\Delta t)=U^q_\eta(\Delta t;t)\phi^q_{\lambda\eta}(t).$$

If Δt is sufficiently small, we may neglect differences due to time ordering and expand the exponential as a series

$$U^q_\eta(\Delta t;t)=1+\sum_{s=1}^{M}[-i\Delta tK^q_\eta(t)]^s/s. \tag{6}$$

For nonlinear time-dependent solutions using Skyrme forces, the optimal choice of the propagator[7] is given by

TABLE I. Definition of the Skyrme II Hamiltonian density as given in Eq. (3).

$$W(\vec{r},t)=t_0\left\{(2+x_0)\rho_p(\vec{r},t)\rho_n(\vec{r},t)+(1-x_0)[\rho_p(\vec{r},t)^2+\rho_n(\vec{r},t)^2]/2\right\}/2$$
$$+(t_1+t_2)\left[\rho(\vec{r},t)\tau(\vec{r},t)-\vec{J}(\vec{r},t)^2\right]/4+(t_2-t_1)\sum_q[\rho_q(\vec{r},t)\tau_q(\vec{r},t)-\vec{J}_q(\vec{r},t)^2]/8$$
$$+\frac{t_3}{4}[\rho_p(\vec{r},t)\rho_n(\vec{r},t)^2+\rho_n(\vec{r},t)\rho_p(\vec{r},t)^2].$$

$$\rho(\vec{r},t)=\rho_p(\vec{r},t)+\rho_n(\vec{r},t),\quad \tau(\vec{r},t)=\tau_p(\vec{r},t)+\tau_n(\vec{r},t),\quad \vec{J}(\vec{r},t)=\vec{J}_p(\vec{r},t)+\vec{J}_n(\vec{r},t),$$
$$\rho_q(r,t)=\sum_\eta \chi_\eta(\vec{r}_\perp)^2R^q_\eta(\vec{r}_\parallel,t)\,\tau_q(\vec{r},t)=\sum_\eta\left[\chi_\eta(\vec{r}_\perp)^2\sum_\lambda|\vec{\nabla}\phi^q_{\lambda\eta}(\vec{r}_\parallel,t)|^2+|\vec{\nabla}\chi_\eta(\vec{r}_\perp)|^2R^q_\eta(\vec{r}_\parallel,t)\right],$$
$$R^q_\eta(r_\parallel,t)=\sum_\lambda|\phi^q_{\lambda\eta}(r_\parallel,t)|^2J_q(r,t)=\sum_\eta\chi_\eta(r_\perp)^2\sum_\lambda\mathrm{Im}\{\phi^q_{\lambda\eta}(r_\parallel,t)\nabla\phi^{q*}_{\lambda\eta}(r_\parallel,t)\}.$$

$t_0=-104.49$ MeV fm^3
$x_0=4.01$
$t_1=+585.6$ MeV fm^5
$t_2=-27.1$ MeV fm^5
$t_3=+9331.0$ MeV fm^5
$a_0=0.459$ fm
$V_L=-444.847$ MeV
$V_u=-863.528$ MeV

$$K^q_\eta(\vec{r}_\parallel,t)=[h^q_\eta(\vec{r}_\parallel;t+\Delta t)+h^q_\eta(\vec{r}_\parallel;t)]/2\quad-\frac{t_3}{8}\int d\vec{r}_\perp\chi_\eta(\vec{r}_\perp)^2$$
$$\times\{\rho(\vec{r};t)^2-\rho(\vec{r};t+\Delta t)^2+\rho_q(\vec{r};t+\Delta t)^2-\rho_q(\vec{r};t)^2$$
$$-2[2\rho_{\bar{q}}(\vec{r};t)\rho_q(\vec{r};t)-\rho_{\bar{q}}(\vec{r};t+\Delta t)\rho_q(\vec{r};t+\Delta t)-\rho_{\bar{q}}(\vec{r};t+\Delta t)\rho_q(\vec{r};t)]\}\,. \tag{7}$$

The presence of the terms involving t_3 in Eq. (7) ensures exact conservation of the total energy. The index $\bar{q}$ denotes the charge state conjugate to q.

The initial static Hartree-Fock wave functions for both ^{16}O and ^{93}Nb can be obtained from Eq. (6) using the imaginary time evolution method.[28] In using this technique, the time interval Δt in the evolution operator [Eq. (6)] is replaced by an imaginary time interval $-i\Delta t$

$$\Delta t\to i\Delta\tau\,,$$
$$\Delta\tau>0\,.$$

In addition, one must also Schmidt orthogonalize the single particle wave functions after each time step. In this way, the time plays the role of an index m, and successive application of the evolution operator corresponds to an iteration sequence which converges to the self-consistent static Hartree-Fock solutions[28]

$$\xi^q_{\lambda\eta}(\vec{r};m+1)=U^q_\eta(-i\Delta t;m)\xi^q_{\lambda\eta}(\vec{r};m)\,. \tag{8}$$

The finite range Skyrme II potential[22,27] in Eq. (3) is spin degenerate and this symmetry is preserved at all times in our calculations. Thus the Hartree-Fock single particle state λ is given in terms of spatial quantum numbers only. The starting guesses for the wave functions before one performs the imaginary time method are products of one dimensional harmonic oscillator functions having quantum numbers μ,ν,

$$\xi^q_{\lambda\eta}(\vec{r}_\parallel)=W_{\lambda\eta q}\chi_\mu(x)\chi_\nu(y),\quad(\vec{r}_\parallel\to\{x,y\})\,. \tag{9}$$

Each Hartree-Fock state λ is specified in terms of the oscillator quantum numbers (η,μ,ν), with a total number of quanta $Q=\eta+\mu+\nu$, and occupation numbers $W^2_{\lambda\eta q}$.

The initial wave function is comprised of two separate static Hartree-Fock wave functions for the target and projectile whose mass centers move along classical Coulomb trajectories in the c.m. frame of the composite system. For the $^{16}_{8}$O projectile the four neutron and four proton levels completely fill the $Q=0$ and 1 shells and result in a spherically symmetric Hartree-Fock wave function. However, for $^{93}_{41}$Nb the exact Hartree-Fock solution is a deformed state, and we employ a static filling approximation to construct a state which is rotationally invariant.

In the $^{93}_{41}$Nb nucleus, 40 protons completely fill the lowest 20 orbitals having quanta $Q=0$, 1, 2, and 3. The remaining proton fractionally occupies

the next lowest level, $(\eta, \mu, \nu) = (2, 1, 1)$. This level is bound in the Hartree-Fock potential by 2.5 MeV. For the neutrons, after filling all of the levels through the $Q = 3$ there remain 12 neutrons to occupy the 15 levels in the $Q = 4$ shell. Two different approximation schemes corresponding to the occupation of the 12 and 15 lowest levels are compared in Table II where the occupation numbers, single particle energies, and binding energies are given. Both solutions are approximately spherically symmetric and the solution having 12 levels gives the lowest energy. The resulting bulk properties of the ^{16}O projectile and ^{93}Nb target are given in Table III. The results obtained using the frozen approximation differ from those obtained with conventional methods using the same two-body interaction, since the former solutions are constrained to be harmonic oscillator functions for the wave function component perpendicular to the reaction plane. The nonzero value of the mass quadrupole moment for the ^{16}O arises because the oscillator parameter $b = 2.20$ fm does not represent a minimum in the ^{16}O Hartree-Fock energy, but corresponds to a minimum for the combined ^{16}O + ^{93}Nb system.

III. RESULTS

We have studied in detail the ^{16}O + ^{93}Nb collision at a laboratory bombarding energy of 204 MeV. At this energy, the reaction cross section is comprised of approximately equal amounts of fusion and deep inelastic scattering. The experimental analysis of this system is presently being carried out[23] and comparisons will be given at the end of this section. In our calculations, the inelastic part of the reaction cross section arises from the principal branches of the deflection function as shown in Fig. 1. The c.m. scattering angle and the outgoing kinetic energy of the fragments are given as a function of the entrance channel angular momentum l. One of the inelastic branches occurs for angular momenta near grazing, for which the damping of the kinetic energy of the fragments is strongly dependent on l. The other branch corresponds to small entrance channel angular momenta, or nearly head-on collisions, for which the outgoing kinetic energy is approximately independent of l. In the ^{16}O + ^{93}Nb system, these two distinct inelastic branches are separated by a region of angular momenta where fusion occurs. We calculate upper and lower limits for fusion $l_>$ and $l_<$, respectively; elastic branches are separated by a region of angular momenta where fusion occurs. We calculate upper and lower limits for fusion $l_>$ and $l_<$, respectively,

$$l_> = 76 \pm 1.0,$$

$$l_< = 30.5 \pm 0.5.$$

The existence of an intermediate range of fusion angular momenta in this way is a characteristic feature of previous TDHF fusion studies of light mass systems.[7-11]

In Fig. 1 the c.m. scattering angle goes to zero for small impact parameters with the subsequent interpretation that in this region the projectilelike fragment "passes through the target." The large angular momentum limit of the TDHF deflection function is compared to the classical deflection function for pure Coulomb scattering (dashed curve). Here one observes that for large l, the TDHF deflection function smoothly goes over to pure Coulomb scattering with the subsequent identification of a classical c.m. Coulomb rainbow angle θ_g and corresponding angular momentum l_g where $d\theta/dl|_{l_g} = 0$. In our study, these are $\theta_g \simeq 14°$ and $l_g \simeq 100 \pm 5$. One should note that this is not the usual $\frac{1}{4}$ point definition for grazing adopted in experimental work.[29]

In Fig. 2 we present the outgoing kinetic energy of the inelastic fragments as a function of the c.m. scattering angle. Each point corresponds to a particular initial angular momentum, the triangles are points from the lower inelastic branch with $l < l_<$, and the circles are those points from the upper inelastic branch with $l > l_>$. The points are joined by a solid line in order to guide the eye. Here the scattering is strongly peaked in the forward direction exhibiting mostly negative angle

TABLE II. Comparison of two different filling approximations for the valence neutrons in ^{93}Nb. The harmonic oscillator length parameter is $b = 2.20$ fm. Both solutions are approximately spherical and the lowest energy solution is used in the present study. Note: $W_\lambda^2 = 1$ does not correspond to unit occupancy because of spin degeneracy.

				$E = -711.6$ MeV		$E = -697.6$ MeV	
λ	η	μ	ν	W_λ^2	E_λ (MeV)	W_λ^2	E_λ (MeV)
1	2	1	1	1.0	−9.7	0.8	−6.6
2	0	2	2	1.0	−8.9	0.8	−6.1
3	1	2	1	1.0	−8.8	0.8	−7.3
4	1	1	2	1.0	−8.8	0.8	−7.3
5	2	0	2	1.0	−7.9	0.8	−5.2
6	2	2	0	1.0	−7.8	0.8	−5.0
7	0	3	1	1.0	−7.8	0.8	−7.6
8	1	0	3	1.0	−7.0	0.8	−6.2
9	1	3	0	1.0	−7.0	0.8	−6.2
10	3	0	1	1.0	−6.6	0.8	−2.4
11	3	1	0	1.0	−6.6	0.8	−2.4
12	0	1	3	1.0	−5.8	0.8	−5.6
13	0	0	4			0.8	−5.1
14	0	4	0			0.8	−5.0
15	4	0	0			0.8	+2.1

TABLE III. Static Hartree-Fock solutions obtained using Eq. (8). The harmonic oscillator length parameter is $b = 2.20$ fm. The imaginary timestep is $\Delta\tau = 0.0025 \times 10^{-21}$ sec.

	$^{16}_{8}O$	$^{93}_{41}Nb$
Binding energy (MeV/nucleon)	−6.744	−7.652
Kinetic energy (MeV/nucleon)	+13.713	+17.283
Nuclear potential energy (MeV/nucleon)	−21.425	−27.777
Finite-range	−27.519	−41.131
Zero-range	+6.094	+13.354
Coulomb potential energy (MeV/nucleon)	+0.969	+2.843
Mass rms radius (fm)	2.850	4.394
Mass quadrupole moment (fm^2)	0.340	0.034

scattering.

As stated previously, we find fusion for those angular momenta between $l_<$ and $l_>$. We adopt the operational definition of fusion established in previous work[7,9-11] and classify as fusion those cases for which the composite system undergoes more than one complete rotation regardless of the subsequent evolution of the system.[16]

In Fig. 3 we display as a function of time the density contours projected on to the reaction plane $l = 70$. We have followed this trajectory for times longer than 2.5×10^{-21} sec. during which the composite system appears to undergo more than three complete rotations.

In Fig. 4 we show as a function of time the rms radius of the system for the angular momentun $l = 0$, 50, and 100. The case $l = 50$ corresponds to fusion, $l = 0$ gives strongly damped inelastic scattering, and $l = 100$ is for a grazing collision. For the latter two cases, the radius rapidly decreases and then increases as the fragments collide and separate with a time which is less than 10^{-21} sec. The fusion case exhibits a similar behavior within the same time scale. For times up to 2×10^{-21} sec the radius slowly increases as the system undergoes rotations and vibrations. For longer times, the radius increases fairly rapidly, even though the corresponding density contours show a compact coalesced system characteristic of TDHF fusion. This rapid increase of the rms radius is due to

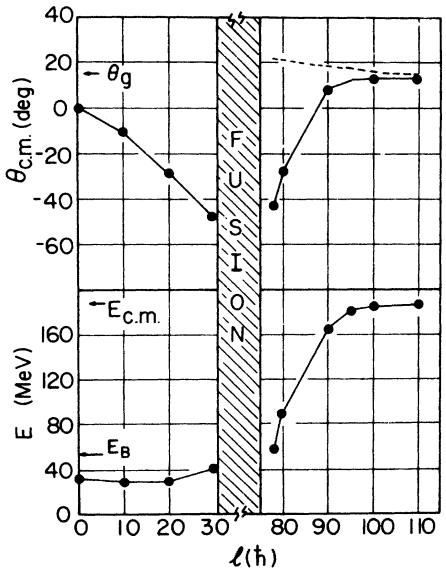

FIG. 1. The c.m. scattering angle in degrees and the outgoing kinetic energy in MeV as a function of the entrance channel angular momenta l. The initial c.m. energy $E_{c.m.}$, the entrance channel Coulomb barrier E_B, and the grazing angle θ_g are indicated on the figure. The dashed curve is the classical Coulomb deflection function for the entrance channel.

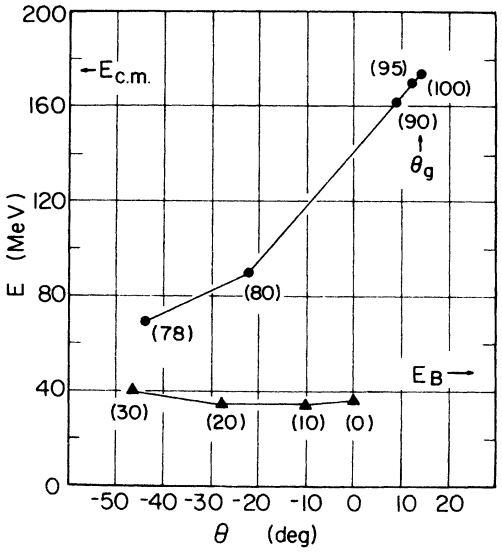

FIG. 2. The outgoing kinetic energy of the inelastic fragments as a function of the c.m. scattering angle. The triangles are the points from the lower branch and the circles the points from the upper inelastic branch. The numbers in parentheses are the entrance channel angular momenta. The quantities $E_{c.m.}$, E_B, and θ_g are shown for comparison.

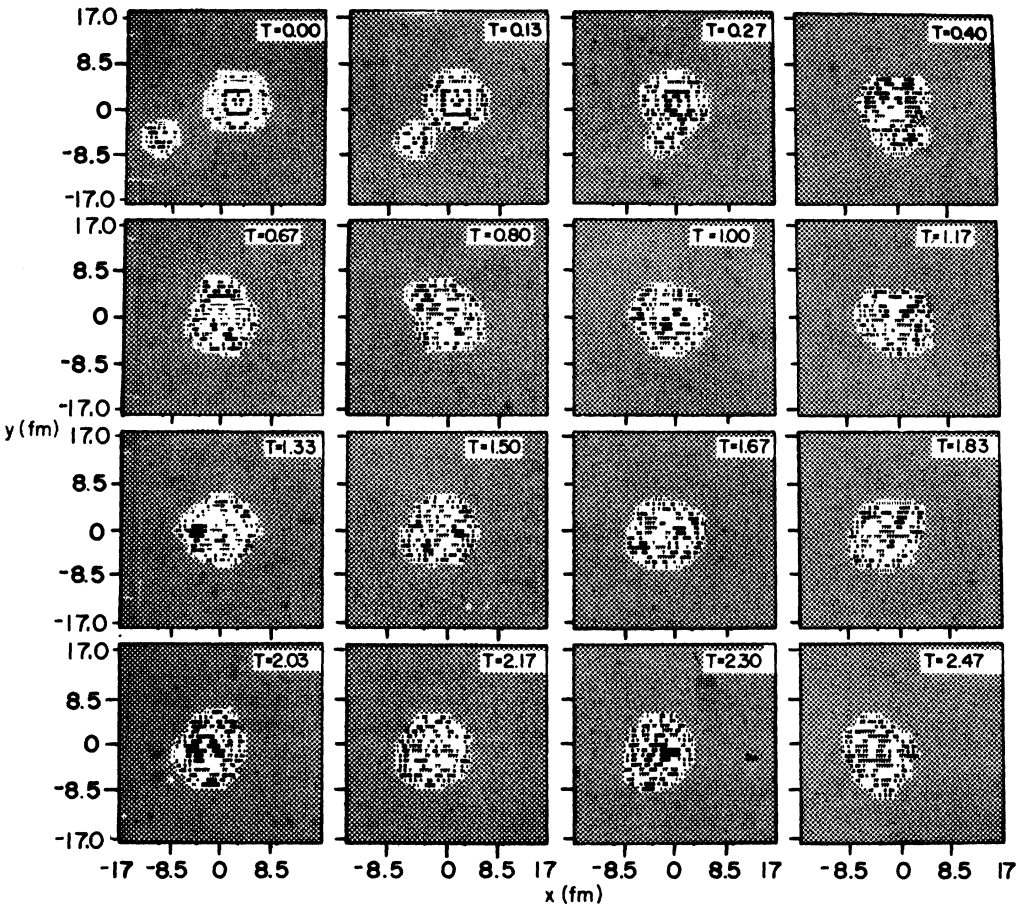

FIG. 3. Density contours in the reaction plane for angular momentum l =70 as a function of time in units of 10^{-21} sec. This is a case which undergoes more than two complete rotations and corresponds to fusion.

a shift of the c.m. of the system induced by the prompt emission of a small number of nucleons.[30] This is in part due to our use of reflective boundary conditions, and in the present work we postpone any detailed investigations of this phenomena since it probably has no direct bearing on the identification of fusion.

In Fig. 5, for the case of head-on collisions ($l = 0$) we show density contours in the reaction plane as a function of time. Here we observe that the projectile like fragment passes through the targetlike fragment. Even though this type of transparency phenomenon is a systematic feature of TDHF fusion studies,[3,11,16] the experimental evidence for its existence is still indirect and inconclusive.[31,32]

In Fig. 6 we show that the outgoing kinetic energy as a function of the average angular momentum excited in the inelastic fragments. The triangles denote those points coming from the lower inelastic branch, and the circles those coming from the upper inelastic branch for angular momenta above fusion. Here one observes a clear separation between the two branches. The lower inelastic branch exhibits a wide range of excited angular momenta focused in a narrow region of outgoing kinetic energy while the upper branch is a strong function of the outgoing kinetic energy. In our model, freezing the degrees of freedom perpendicular to the reaction plane yields a mean angular momentum aligned perpendicular to the reaction plane. This approximation is consistent with the classical model calculations of Vandenbosch[33] which show that most of the angular momenta transferred in deep inelastic scattering is aligned perpendicular to the reaction plane. In the work of Vandenbosch, the mechanism for angular momentum transfer is particle exchange.

In Fig. 7 we compare the angular momentum transfer and the mean projectilelike mass as a function of the entrance channel angular momentum l. For the upper inelastic branch we find that the angular momentum transfer increases as particle transfer from the projectile to the target in-

FIG. 4. The rms radius of the composite system as a function of time for three different angular momenta.

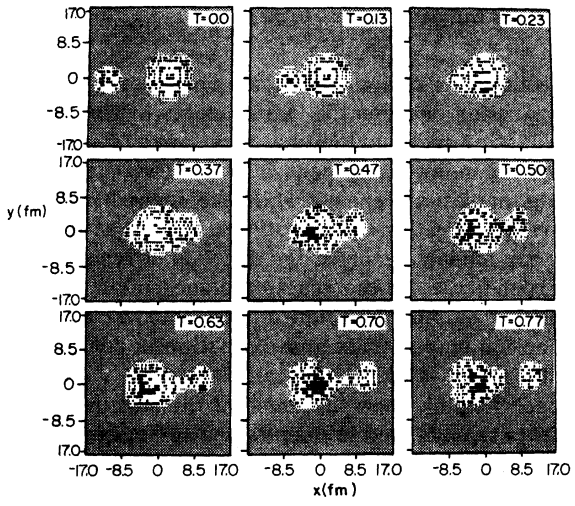

FIG. 5. Density contours in the reaction plane for angular momentum $l = 0$ as a function of time in units of 10^{-21} sec. This is an example from the lower inelastic branch in which the projectilelike fragment passes through the targetlike fragment. (Note that the density contours are not symmetric about $Y = 0$ because of small interpolation differences in the plotting program.)

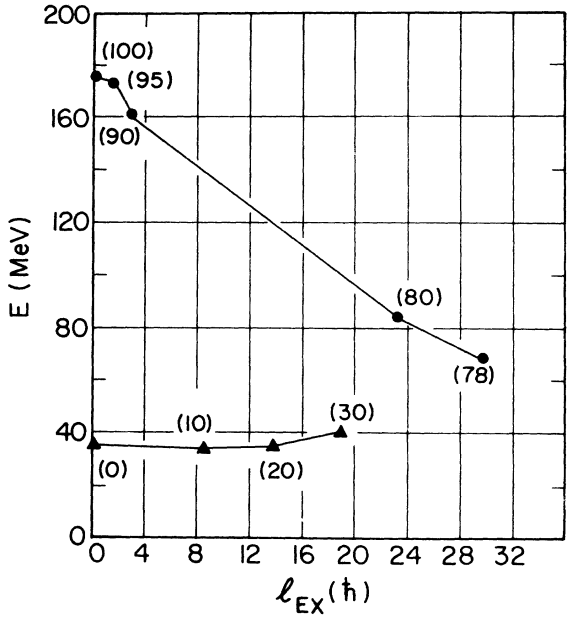

FIG. 6. The outgoing kinetic energy of the inelastic fragments as a function of the mean angular momentum excited in the fragments. The triangles are the points from the lower inelastic branch and the circles those from the upper inelastic branch. The number in parentheses is the initial angular momentum for each point.

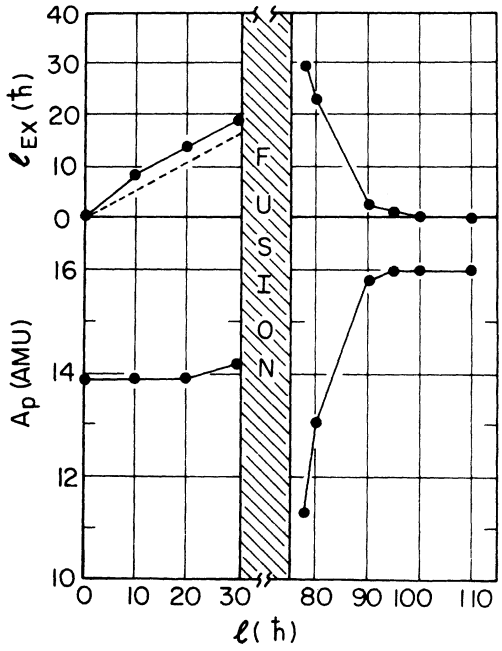

FIG. 7. The mean angular momentum transferred and projectilelike fragment mass as a function of the entrance channel angular momentum l. The dashed curve is the angular momentum excited in the fragments using the macroscopic model discussed in the text.

creases. However, for the lower inelastic branch, as we decrease l, we observe that angular momentum transfer decreases as the mean projectilelike mass is roughly constant, possibly suggesting that particle transfer has equilibrated and that angular momentum transfer decreases as the total angular momentum available decreases. In Fig. 7 we also compare the angular momentum excited in the fully damped fragments with that obtained using a simple macroscopic model (dashed curves). In this model[34] one envisions frictional forces acting between the fragments to slow down the rotation until a rigid "sticking" configuration is obtained. The total internal angular momentum l_{ex} is then given by the expression

$$l_{ex} = \frac{\mathcal{I}_1 + \mathcal{I}_2}{\mu R^2 + \mathcal{I}_1 + \mathcal{I}_2} l ,$$

where $\mathcal{I}_1$ and $\mathcal{I}_2$ are the moments of inertia of the two fragments (assumed spherical), μ is the reduced mass, and R the separation of the centers of the two fragments at scission. In the $^{16}O + ^{93}Nb$ system this gives

$$l_{ex} \simeq 0.54 l ,$$

which is the dashed line. One should note that the above simple model neglects angular momentum transfer induced by mass transfer, and is in reasonably good agreement with the TDHF results for the lower branch in which the particle transfer in TDHF appears equilibrated.

Using the sharp cutoff approximation,[7,9] we calculate the reaction, fusion, and total inelastic cross sections (σ_r, σ_f, and σ_i, respectively) for the cases shown in Fig. 1. The inelastic cross section can be divided into the partially damped component $\sigma_>$ and the fully damped component $\sigma_<$

$$\sigma_i = \sigma_< + \sigma_> ,$$

$$\sigma_< = \frac{\pi}{K^2} \sum_{l=0}^{l_<} (2l+1) ,$$

$$\sigma_> = \frac{\pi}{K^2} \sum_{l=l_>}^{l_g} (2l+1) .$$

The fusion cross section arises from those angular momenta between $l_<$ and $l_>$,

$$\sigma_f = \frac{\pi}{K^2} \sum_{l=l_<}^{l_<} (2l+1) ,$$

and the reaction cross section only depends on the grazing angular momentum l_g,

$$\sigma_r = \frac{\pi}{K^2} \sum_{l=0}^{l_g} (2l+1) ,$$

where in the above the relative wave number is given in terms of the reduced mass μ and the c.m. energy $E_{c.m.}$

$$K^2 = 2\mu E_{c.m.} .$$

Our TDHF results are compared with the experimental data of Ref. 23 in Table IV and in Fig. 8. In Table IV, the experimental grazing angle and grazing angular momenta are obtained using the $\frac{1}{4}$ point method of Ref. 29. The TDHF total reaction, inelastic, and fusion cross sections are in general agreement with the corresponding experimental quantities. In Fig. 8 the experimental cross section, $(d^2\sigma/d\Omega\, dE_{lab})_{lab}$ is shown as a function of the outgoing laboratory kinetic energy of the fragments and their corresponding laboratory scattering angles. The TDHF outgoing kinetic energies and scattering angles in the laboratory frame are obtained from the corresponding c.m. quantities in Fig. 2 using the final masses from Fig. 7. All TDHF energies below about $E_{lab} \simeq 175$ MeV correspond to negative angle scattering and have been reflected to positive angles to compare with the experimental data. The dashed part of the TDHF curve are those points from the upper inelastic branch while the solid part of the curve comes from the lower inelastic branch. From these comparisons, we conclude that the TDHF results are in general agreement with the experimental data.

IV. SUMMARY

We have carried out TDHF calculations of the $^{16}O + ^{93}Nb$ system at a laboratory bombarding energy of $E_{lab} = 204$ MeV using the 2D frozen approximation.[4,5] This approximation is known to give very good results in light systems when compared to fully 3D calculations using Skyrme type local potentials. In our work we have employed the finite-range nonlocal Skyrme II interaction and have treated neutron and proton single particle wave

TABLE IV. Summary of scattering results and comparison with experiment.

	Quantity	TDHF	Experiment[a]
$l_<$	($\hbar$)	30.5 ± 0.5	
$l_>$	($\hbar$)	76.5 ± 1.5	
l_g	($\hbar$)	100.0 ± 5.0	98
θ_g	(deg)	14	16
$\sigma_<$	[b](mb)	271 ± 9	
$\sigma_>$	[c](mb)	1220 ± 277	
σ_i	(mb)	1492 ± 286	1354
σ_f	(mb)	1375 ± 73	1350
σ_r	(mb)	2853 ± 326	2704

[a] Reference 23.
[b] Fully damped.
[c] Partially damped.

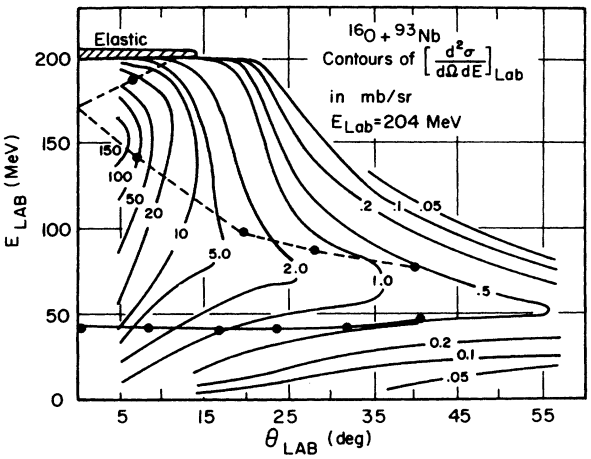

FIG. 8. Comparison of the experimental contours of $[d^2\sigma/d\Omega dE]_{lab}$ (Ref. 23) with the TDHF results. The solid circles refer to TDHF inelastic scattering, with results for angular momenta above fusion connected by a dashed curve, and results for angular momenta below fusion connected by a solid curve.

functions separately. We have ignored the spin-orbit part of the interaction so that spin-up states are degenerate with spin-down states. For the ^{93}Nb target we have used a static filling approximation for non-closed shells, and thus in our calculations Nb does not have the correct stiffness with respect to deformations. At this energy, we find 45% of the total reaction cross section is fusion and 55% is inelastic scattering. Fusion occurs in an angular momentum region between two branches of strongly damped inelastic scattering. The lower branch comprises 16% of the total inelastic cross section and extends from $l = 0$ to $l = 30$. The upper branch extends from $l = 78$ to the grazing angular momentum $l_g = 100 \pm 5$. The grazing angle is 14° in the center of mass and the inelastic scattering is peaked in the forward direction. We calculate the mean angular momentum excited in the fragments as a function of the outgoing kinetic energy and observe that this quantity has a different behavior in the different inelastic branches. This suggests that the experimental determination of this quantity may help to prove or disprove the existence of the TDHF transparency window.

ACKNOWLEDGMENTS

This research was sponsored in part by the Division of Basic Energy Sciences, U. S. Department of Energy under Contract No. W-7405-ENG-26 with the Union Carbide Corporation, and under Contract No. AC02-76ER03074 with Yale University, and by the National Science Foundation under Contract No. PHY77-21602. Our computations were performed at the SRC Daresbury Laboratory on the Cray-1 Computer System. Support by the Daresbury Laboratory and assistance of members of the Computer Systems and Electronics Division is gratefully acknowledged. Stimulating discussions with Dr. F. Obenshain, Dr. R. L. Ferguson, Dr. A. Gavron, Dr. F. Plasil, Dr. G. R. Young, Dr. S. E. Koonin, and Dr. D. M. Brink are acknowledged.

[1]P. Bonche, S. Koonin, and J. W. Negele, Phys. Rev. C 13, 1226 (1976).
[2]S. E. Koonin, K. T. R. Davies, V. Maruhn-Rezwani, H. Feldmeier, S. J. Krieger, and J. W. Negele, Phys. Rev. C 15, 1359 (1977).
[3]K. T. R. Davies and S. E. Koonin (unpublished).
[4]S. E. Koonin, B. Flanders, H. Flocard, and M. S. Weiss, Phys. Lett. 77B, 13 (1978).
[5]K. R. Sandhya Devi and M. R. Strayer, J. Phys. G 4, L97 (1978); Phys. Lett. 77B, 135 (1978); K. R. Sandhya Devi, M. R. Strayer, and J. M. Irvine, J. Phys. G 5, 281 (1979).
[6]R. Y. Cusson, R. K. Smith, and J. Marahun, Phys. Rev. Lett. 36, 1166 (1976); R. Y. Cusson, J. A. Maruhn, and H. W. Meldner, Phys. Rev. C 18, 2589 (1978).
[7]H. Flocard, S. E. Koonin, and M. S. Weiss, Phys. Rev. C 17, 1682 (1978); P. Bonche, B. Grammaticos, and S. E. Koonin, *ibid.* 17, 1700 (1978).
[8]V. Maruhn-Rezwani, K. T. R. Davies, and S. E. Koonin, Phys. Lett. 67B, 134 (1976).
[9]S. J. Krieger and K. T. R. Davies, Phys. Rev. C 18, 2567 (1978); 20, 167 (1979).
[10]K. T. R. Davies, H. T. Feldmeier, H. Flocard, and M. S. Weiss, Phys. Rev. C 18, 2631 (1978).
[11]P. Bonche, K. T. R. Davies, B. Flanders, H. Flocard, B. Grammaticos, S. E. Koonin, S. J. Krieger, and M. S. Weiss, Phys. Rev. C 20, 641 (1979).
[12]K. T. R. Davies, V. Maruhn-Rezwani, S. E. Koonin, and J. W. Negele, Phys. Rev. Lett. 41, 632 (1978).
[13]A. K. Dhar and B. S. Nilsson, Phys. Lett. 77B, 50 (1978); A. K. Dhar, Phys. Rev. Lett. 42, 1124 (1979).
[14]R. Y. Cusson and H. W. Meldner, Phys. Rev. Lett. 42, 694 (1979); R. Y. Cusson, H. W. Meldner, and H. Stöcker, Z. Phys. A294, 257 (1980).
[15]K. T. R. Davies, K. R. Sandhya Devi, and M. R. Strayer, Phys. Rev. C 20, 1372 (1979).
[16]K. T. R. Davies, K. R. Sandhya Devi, and M. R. Strayer, Phys. Rev. Lett. 44, 23 (1980); unpublished.
[17]B. Flanders, P. Bonche, S. E. Koonin, and M. S. Weiss (unpublished).
[18]A. K. Dhar, B. S. Nilsson, and K. T. R. Davies (unpublished).
[19]C. H. Dasso, T. Døssing, and H. C. Pauli, Z. Phys. A 289, 395 (1979).
[20]R. Vandenbosch, private communication.

[21]W. V. Schröder and J. R. Huizenga, Ann. Rev. Nucl. Sci. 27, 465 (1977).
[22]J. R. Birkelund, L. E. Tubbs, J. R. Huizenga, J. N. De, and D. Sperber, Phys. Rep. 56, 107 (1979).
[23]F. Obenshain, R. L. Ferguson, F. Plasil, A. H. Snell, and G. R. Young (unpublished).
[24]J. W. Negele, S. E. Koonin, P. Möller, J. R. Nix, and A. J. Sierk, Phys. Rev. C 17, 1098 (1978).
[25]K. R. Sandhya Devi and M. R. Strayer (unpublished).
[26]A. K. Kerman and S. E. Koonin, Ann. Phys. (N. Y.) 100, 332 (1976).
[27]P. Hoodbhoy and J. W. Negele, Nucl. Phys. A288, 23 (1977).
[28]K. T. R. Davies, H. Flocard, S. J. Krieger, and M. S. Weiss, Nucl. Phys. A342, 111 (1980).
[29]J. S. Blair, Phys. Rev. 95, 1218 (1954).
[30]K. T. R. Davies, K. R. Sandhya Devi, M. R. Strayer, and A. K. Dhar (unpublished).
[31]J. B. Natowitz, G. Doukellis, B. Kolb, G. Rosner, and Th. Walcher (unpublished).
[32]A. Lazzarini, H. Doubre, K. Lesko, V. Metag, A. Scamaster, and R. Vandenbosch, in *Proceedings of the Workshop on Nuclear Dynamics, Granlibakkan, California, 1980,* Lawrence Berkeley Laboratory, Report No. LBL-10688.
[33]R. Vandenbosch, Phys. Rev. C 20, 171 (1979).
[34]P. Glässel, R. S. Simon, R. M. Diamond, R. C. Jared, I. Y. Lee, L. G. Moretto, J. W. Newton, R. Schmitt, and F. S. Stephens, Phys. Rev. Lett. 38, 331 (1977).

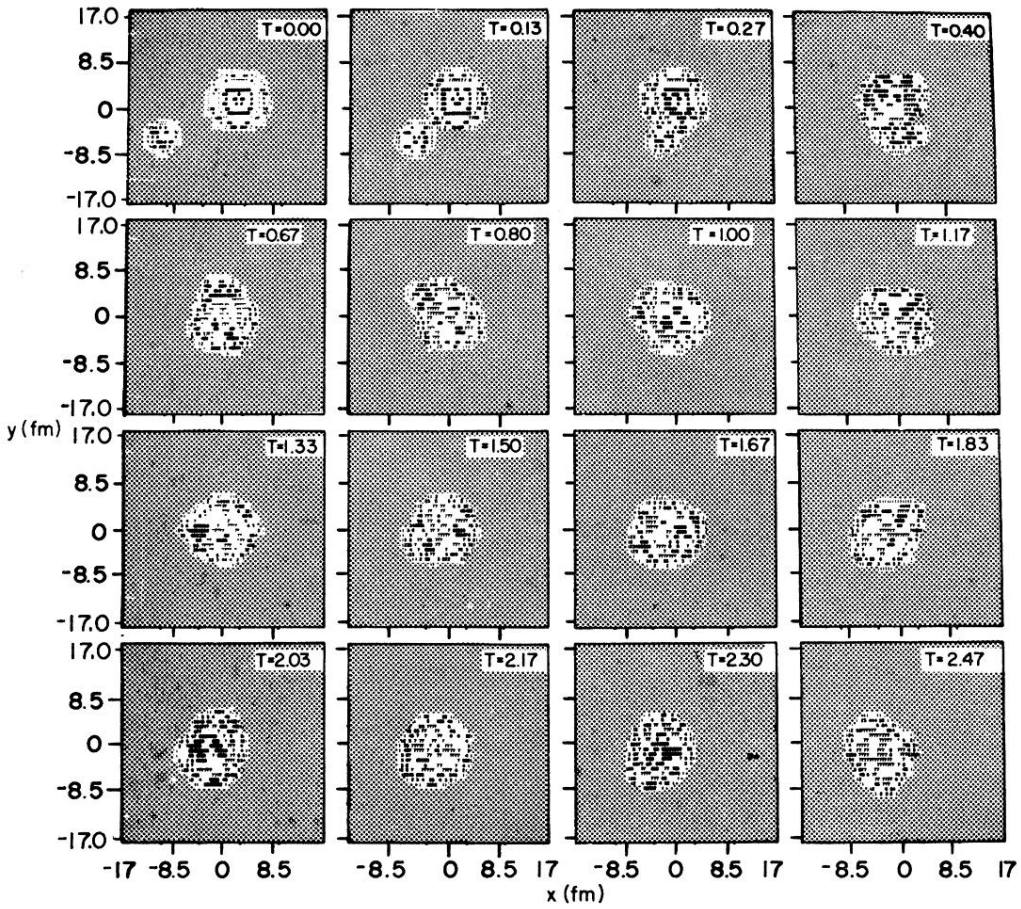

FIG. 3. Density contours in the reaction plane for angular momentum $l = 70$ as a function of time in units of 10^{-21} sec. This is a case which undergoes more than two complete rotations and corresponds to fusion.

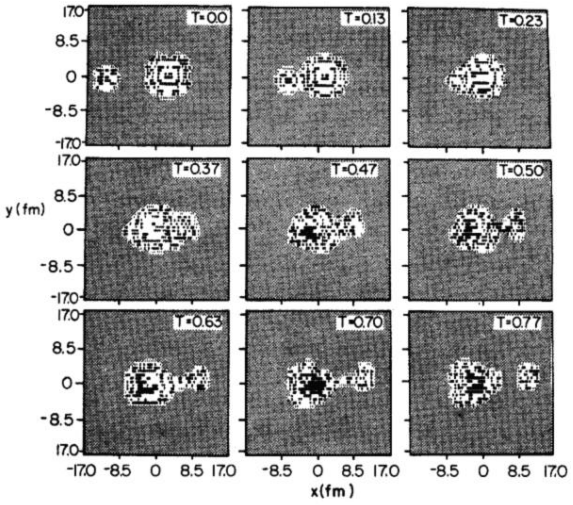

FIG. 5. Density contours in the reaction plane for angular momentum $l = 0$ as a function of time in units of 10^{-21} sec. This is an example from the lower inelastic branch in which the projectilelike fragment passes through the targetlike fragment. (Note that the density contours are not symmetric about $Y = 0$ because of small interpolation differences in the plotting program.)